Research Square

Preprints are preliminary reports that have not undergone peer review.
They should not be considered conclusive, used to inform clinical practice,
or referenced by the media as validated information.

Certified anisotropic meshing of thin, high-aspect-ratio regions in device modeling

Hakeim Talleb

hakeim.talleb@sorbonne-universite.fr

Sorbonne Université

Aboubaker Elomari

Sorbonne Université

Mohamed Ben Chouikha

Sorbonne Université

Research Article

Keywords: Anisotropic mesh, Thin layers, A posteriori error bounds, Complementary energy, Raviart–Thomas elements, Device simulation

Posted Date: November 6th, 2026

DOI: https://doi.org/10.21203/rs.3.rs-11367763/v1

License: This work is licensed under a Creative Commons Attribution 4.0 International License.
Read Full License

Additional Declarations: No competing interests reported.

Certified anisotropic meshing of thin, high-aspect-ratio regions in device modeling

Hakeim Talleb[1*], Aboubaker Elomari[1] and Mohamed Ben Chouikha[1]

[1*]Sorbonne Université, CNRS, Laboratoire de Génie Electrique et Electronique de Paris, 75252, Paris, France; Université Paris-Saclay, CentraleSupélec, CNRS, Laboratoire de Génie Electrique et Electronique de Paris, 91192, Gif-sur-Yvette, France.

*Corresponding author(s). E-mail(s): hakeim.talleb@sorbonne-universite.fr;

Abstract

Thin layers embedded in much larger bodies are routine in semiconductor devices and a chronic difficulty for device simulation. A mesher that keeps elements near-isotropic must resolve the layer thickness in the plane as well, so the number of unknowns grows as the square of the layer aspect ratio. We resolve the layer instead with anisotropic structured cells, whose count does not depend on the aspect ratio, and we certify the result. For steady conduction, a conforming P1 potential and an equilibrated Raviart–Thomas flux, computed on the same mesh, enclose the exact resistance between guaranteed bounds without any reference solution. The enclosure width depends on how planar the field is, not on element shape. For layer-parallel flow it is at round-off level, below $\mathbf{10^{-11}}$, for cell aspect ratios from 10:1 to 1000:1. For a 10 mm wide, 30 µm thick film, 567 nodes then give the exact sheet conductance, where an isotropic mesh would need about $\mathbf{1.6 \times 10^{7}}$ nodes. For a point source on a 30 nm film over a substrate, the anisotropic solution matches the closed-form image series to within 0.14% once the grounded outer boundary is accounted for. For a contact on a film–substrate structure, the certified enclosures are nested and shrink from 23% to 6.9% under refinement. Applied to a three-layer stack, the method shows that a 30 nm sheet, 0.5% of the total thickness, carries 0.13% or 13.4% of the potential drop depending on its doping, and the certified enclosures of the access resistance for the two dopings are disjoint.

Keywords: Anisotropic mesh, Thin layers, A posteriori error bounds, Complementary energy, Raviart–Thomas elements, Device simulation

1 Introduction

Device simulation predicts the electrical figures of merit of a structure before any wafer is processed, and its predictive value rests on the accuracy of the discrete solution [1–3]. Most device meshers build near-isotropic, Delaunay-conforming elements adapted to the local feature size [4, 5], because classical finite-element and finite-volume error estimates degrade when elements become flat or needle-like [6, 7]. The interplay between the mesh and the discretization is a known source of error in three-dimensional device and process simulation [8], and adaptive strategies have been developed to control it [9].

A recurring class of structures combines a very thin layer with a large lateral extent. Multi-gate and thin-body transistors confine the channel to films thinner than 10 nm [10]. Two-dimensional semiconductors reduce the channel to a monolayer

[11], and oxide thin-film transistors use active layers tens of nanometres thick over centimetre-scale panels [12]. Stacked-photodiode colour and multispectral sensors separate their diodes by doped isolation sheets tens of nanometres thick across pixels micrometres wide [13, 14]. Electrical test structures (four-point probes, van der Pauw and Hall crosses) characterise films micrometres thick patterned over millimetre-sized dies [15, 16]. In each case one dimension sits two to five orders of magnitude below the others (Fig. 1).

Two strategies are in use for such layers. The first removes the layer from the mesh and replaces it by an interface condition or a compact sheet model, which is cheap but carries an error that cannot be bounded, since the model is calibrated on simulations that did not resolve the layer. The second resolves the layer with elements stretched along it. Anisotropic meshing is well established in computational mechanics and fluid dynamics [17–20], together with a posteriori estimators adapted to stretched elements [21–23]. These estimators, however, contain constants that depend on the alignment of the mesh with the solution, so they indicate the error rather than bound it.

This paper makes the second route accountable for the linear conduction problems that underlie resistance, sheet-resistance and access-resistance extractions; the nonlinear equilibrium of doped layers is discussed in Section 4. We combine anisotropic structured cells with a certificate based on complementary energy: a conforming potential and an equilibrated flux, computed on the same mesh, enclose the exact resistance between two computed numbers. This is the Prager–Synge hypercircle [24, 25], long used in electromagnetism as the dual-energy method [26, 27] and underlying modern guaranteed and equilibrated a posteriori estimators [28–34]. We show that this enclosure is the one that survives extreme element stretching: it is exact for layer-parallel flow at any aspect ratio, and it reports the residual error where the field redistributes. Section 2 states the cost model and the certificate, Section 3 validates the method against three closed-form references and applies it to a three-layer stack, and Section 4 positions it with respect to existing anisotropic estimators.

2 Method

2.1 Cost of an isotropic mesh

Away from junctions, the extractions considered here reduce to steady conduction on a piecewise-uniform medium,

$$\nabla \cdot (\sigma \nabla V) = 0 \text{ in } \Omega, \qquad V = V_k \text{ on contact } \Gamma_k, \tag{1}$$

with homogeneous Neumann conditions elsewhere. A layer of thickness e_1 lies on a body of thickness e_2, and the structure spans a lateral size $W \gg e_1$. A mesher that resolves the layer with m near-isotropic cells across its thickness uses a step $h = e_1/m$ in all three directions, so the number of nodes scales as

$$\begin{aligned} N_{\text{iso}} &\sim \left(\frac{W}{h}\right)^2 \frac{e_1 + e_2}{h} \\ &= m^3 A^2 \, \frac{e_1 + e_2}{e_1}, \qquad A = \frac{W}{e_1}. \end{aligned} \tag{2}$$

For the reference structure of Table 1 ($W = 10$ mm, $e_1 = 30$ µm, $e_2 = 500$ µm, $m = 2$), Eq. (2) gives $N_{\text{iso}} \approx 1.6 \times 10^7$ nodes. The cost is set by the isotropy of the mesh, not by the physics.

2.2 Anisotropic structured cells

Away from contacts and layer edges, the field in a near-planar layer is almost one-dimensional and varies on the lateral scale W, not on e_1. We therefore discretize the structure as the tensor product of a coarse lateral grid ($n_x \times n_y$) with a graded vertical grid (n_{z1} cells in the layer, n_{z2} in the body), and split each hexahedron into six tetrahedra by the Kuhn–Freudenthal subdivision [35]. A layer cell then has aspect ratio

$$a_{\text{cell}} = \frac{W/n_x}{e_1/n_{z1}}, \tag{3}$$

taken here between 10:1 and 1000:1, and the node count

$$N_{\text{aniso}} = (n_x + 1)(n_y + 1)(n_{z1} + n_{z2} + 1) \tag{4}$$

does not depend on A (Fig. 2). For the reference structure, $n_x = n_y = 8$, $n_{z1} = 2$, $n_{z2} = 4$ give 567 nodes and 2304 tetrahedra, with $a_{\text{cell}} = 83$. Classical a priori estimates on such cells rely on angle

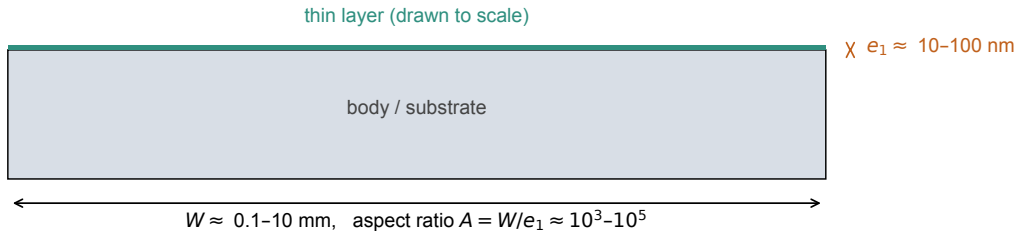


Fig. 1 A thin layer in a larger body, drawn to scale. The layer thickness e_1 is 10 to 100 nm and the lateral size W is 0.1 to 10 mm, so the aspect ratio $A = W/e_1$ ranges from 10^3 to 10^5

conditions [6, 7] or on the alignment of the cells with the solution [17], so a single conforming solution on this mesh comes with no computable error bound. Sections 2.3 and 2.4 replace that guarantee by a computed one.

2.3 The certificate: a two-sided enclosure

For a two-terminal problem with unit voltage between Γ_A and Γ_B, the conductance G is the minimum of the Dirichlet energy over admissible potentials and the inverse of the minimum of the complementary energy over admissible currents. On the same mesh we compute a conforming P1 potential V_h, whose energy bounds G from above,

$$G_{\mathrm{up}} = \int_\Omega \sigma \, |\nabla V_h|^2 \, \mathrm{d}\Omega \;\geq\; G, \tag{5}$$

and a lowest-order Raviart–Thomas current $\mathbf{j}_h \in H(\mathrm{div})$ [36, 37], divergence-free and carrying unit current from Γ_A to Γ_B, whose complementary energy bounds G from below,

$$G_{\mathrm{lo}} = \left[\int_\Omega \rho \, |\mathbf{j}_h|^2 \, \mathrm{d}\Omega \right]^{-1} \leq\; G, \qquad \rho = 1/\sigma. \tag{6}$$

The resistance $R = 1/G$ is therefore enclosed as

$$R_{\mathrm{lo}} = \frac{1}{G_{\mathrm{up}}} \;\leq\; R \;\leq\; \frac{1}{G_{\mathrm{lo}}} = R_{\mathrm{up}}, \tag{7}$$

without any reference solution, and the relative width

$$\eta = \frac{R_{\mathrm{up}} - R_{\mathrm{lo}}}{R_{\mathrm{up}}} \tag{8}$$

bounds the relative discretization error of either estimate. The pair of Eqs. (5) and (6) is the primal–dual pairing of the discrete geometric approach [38, 39]. It rests on the hypercircle identity [24, 25], which makes η a guaranteed quantity rather than an estimate with an unknown constant [28, 32].

2.4 Why the certificate survives stretching

The width η is set by the distance of each discrete field from the exact one, not by element shape. When the flow is purely layer-parallel or purely through-thickness, the exact potential is piecewise linear along the mesh columns and the exact current is piecewise constant. The P1 and RT0 spaces then contain the exact fields, both bounds are exact, and $\eta = 0$ at any a_{cell}. The parallel-sheet conductance of a film on a body driven by full side contacts,

$$G_{\mathrm{exact}} = \frac{\sigma_1 e_1 + \sigma_2 e_2}{L} \, W_y, \tag{9}$$

tests this property directly. Where the current redistributes vertically, near contacts and layer edges, the discrete fields depart from the exact ones, η becomes positive, and Eq. (8) reports how much refinement is needed. The geometry in which an isotropic mesh is most expensive is therefore the one in which the enclosure is tightest on stretched cells.

2.5 Implementation

The P1 problem is assembled on the Kuhn tetrahedra and solved with a sparse direct solver. The RT0 problem is solved in mixed form for the face fluxes and the element-wise potential multipliers, with the contact potentials entering as natural boundary data and zero normal flux on the other

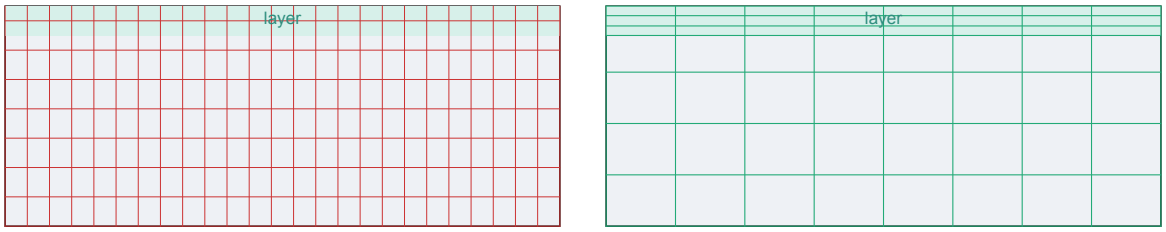


Fig. 2 Two discretizations of a thin layer on a thick body. (a) An isotropic mesh uses the layer step in the whole plane, so $N \propto A^2$, Eq. (2). (b) Anisotropic structured cells use two to four flat cells across the layer and a coarse lateral grid, so N does not depend on A, Eq. (4)

boundary faces. At the discrete optimum the complementary energy equals the computed terminal current I_h, so the flux normalized to unit current gives $G_{\mathrm{lo}} = I_h$ in Eq. (6). The mixed problem is solved on the mesh scaled to unit size, which improves its conditioning without changing G. Axisymmetric problems (Section 3.2) use the same P1 construction on a graded (r, z) triangulation with the weight $2\pi r$. Contacts are unions of mesh faces, chosen to lie on grid lines for every mesh in a refinement sequence, so that every enclosure in the sequence refers to the same continuous problem. The equilibrium band diagrams of Section 3.4 come from a one-dimensional Poisson–Boltzmann solver (Newton iterations, tridiagonal solve). All computations run in double precision in Python with NumPy and SciPy. The scripts were written with the help of a generative AI coding assistant. They are deterministic, every number and figure in this paper is regenerated by them, and they are publicly available (see Code availability). The authors checked all derivations and results.

3 Results

Every enclosure below comes from the two complementary solutions on one mesh. Where a closed form exists, it is used only afterwards, to check that it lies inside the enclosure. Table 1 lists the parameters of the four test problems.

3.1 Layer-parallel flow: exact on stretched cells

Problem 1 drives a conductive film on a resistive body through full side contacts, so the flow

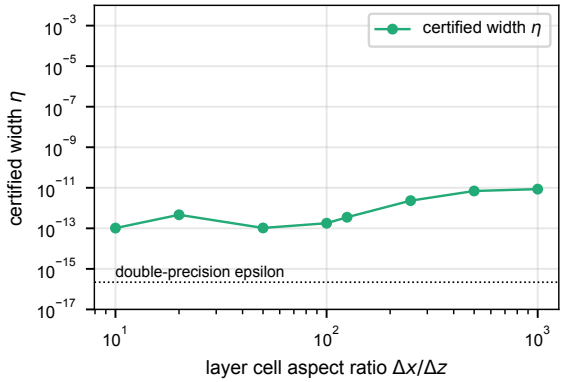


Fig. 3 Problem 1: certified width η, Eq. (8), versus layer cell aspect ratio for the parallel-sheet benchmark, Eq. (9). The width stays at round-off level up to 1000:1

is layer-parallel and Eq. (9) gives the exact conductance. Table 2 and Fig. 3 report the enclosure width for cell aspect ratios from 10:1 to 1000:1. The width stays between 1.0×10^{-13} and 8.6×10^{-12}. These values are set by floating-point round-off in the linear solves, which grows with the condition number of the stretched system, and not by discretization: both bounds coincide with G_{exact} to the same relative level. The 1000:1 case uses 240 tetrahedra. For the reference structure (problem 1'), 567 nodes and 2304 tetrahedra with $a_{\mathrm{cell}} = 83$ give $R_{\mathrm{lo}} = R_{\mathrm{up}} = 0.285714\ \Omega$ with $\eta = 1.5{\times}10^{-12}$, equal to $1/G_{\mathrm{exact}}$, against $1.6{\times}10^{7}$ nodes for the isotropic mesh of Eq. (2), a factor 2.8×10^{4} in unknowns.

3.2 Two-dimensional field: point source on a thin film

Layer-parallel flow tests the cost of the anisotropic mesh but not its fidelity on a two-dimensional

Table 1 Test problems. Conductivities in $\mathrm{S\,m^{-1}}$; problems 1 and 2 are non-dimensional in length

Problem (Section)	Geometry	Layer	Body	Contacts
1 Parallel sheet (3.1)	3D, $W = 1$	$e_1 = 0.002$, $\sigma_1 = 5$	$e_2 = 0.10$, $\sigma_2 = 1$	full side faces
1' Reference (3.1)	3D, $W = 10$ mm	$e_1 = 30$ µm, $\sigma_1 = 10^5$	$e_2 = 500$ µm, $\sigma_2 = 10^3$	full side faces
2 Point source (3.2)	axisym., $R_{\max} = 100$ µm	$e_1 = 30$ nm, $\sigma_1 = 100$	$e_2 = 100$ µm, $\sigma_2 = 1$	disk of radius 7.5 nm
3 Film contact (3.3)	3D, $W = 1$	$e_1 = 0.03$, $\sigma_1 = 100$	$e_2 = 0.5$, $\sigma_2 = 1$	square $[0.3W, 0.7W]^2$ / bottom and walls
4 Three-layer stack (3.4)	axisym. ($R_{\max} = 20$ µm) and 3D ($W = 10$ µm)	30 nm sheet, $\sigma = 1280$ or 2.16	300 nm, $\sigma = 200$, over 6 µm, $\sigma = 21.6$	disk (200 nm) or square / bottom and walls

Table 2 Problem 1: enclosure width versus layer cell aspect ratio

a_{cell}	n_x, n_{z1}, n_{z2}	tetrahedra	η
10:1	50, 1, 2	45000	1.0×10^{-13}
20:1	25, 1, 2	11250	4.7×10^{-13}
50:1	10, 1, 2	1800	1.0×10^{-13}
100:1	5, 1, 4	750	1.8×10^{-13}
125:1	8, 2, 4	2304	3.5×10^{-13}
250:1	4, 2, 4	576	2.3×10^{-12}
500:1	4, 4, 6	960	6.9×10^{-12}
1000:1	2, 4, 6	240	8.6×10^{-12}

field. Problem 2 injects a current I at the surface of a film of thickness e_1 and conductivity σ_1 on a substrate of conductivity σ_2. For a semi-infinite substrate the surface potential is the image series [15, 16]

$$V(r) = \frac{I}{2\pi\sigma_1}\left[\frac{1}{r} + 2\sum_{n\geq 1}\frac{k^n}{\sqrt{r^2 + (2ne_1)^2}}\right], \qquad k = \frac{\sigma_1 - \sigma_2}{\sigma_1 + \sigma_2}. \tag{10}$$

The current enters the film, spreads in it and leaks into the substrate, so the field is fully two-dimensional. The axisymmetric mesh has 3910 nodes and 7560 triangles, with 5 cells across the 30 nm film and film cells up to 49 times wider than thick within 3 µm of the source. Fig. 4 compares the computed surface potential with Eq. (10), summed to 2000 terms. The deviation is −0.69% at $r = e_1$, −1.32% at $r = 10e_1$ and −2.87% at $r = 60e_1$. It is dominated by the truncation of the domain: the computation grounds the boundary at $R_{\max} = 100$ µm, where Eq. (10) still gives 1590 V for $I = 1$ A. Compared with $V(r) - V(R_{\max})$, the deviation is at most 0.14% over the whole range. Moving the boundary to 400 µm lowers the raw deviation to at most 0.95%. The film cells, stretched up to 49:1, therefore add an error of the order of 0.1%.

3.3 Certified access resistance of a contact

Problem 3 injects current through a square contact on top of the film and collects it on the bottom and side walls. The current crowds under the contact edges, so the enclosure has a finite width. Table 3 and Fig. 5a report it on four meshes whose contact edges lie on grid lines. Each interval encloses the same exact resistance, the intervals are nested, and the width falls from 22.9% to 6.9% as the mesh grows from 4800 to 144000 tetrahedra. Their intersection, $R \in [0.04290, 0.04606]$, is itself guaranteed. The width decreases as $n_x^{-0.87}$, a rate set by the singularity of the current at the contact edges rather than by the stretched cells: the layer-parallel case of Section 3.1 gave a zero width on a coarser mesh. The uniform refinement used here is the simplest choice; the local contributions to η, which concentrate at the contact edges, are the natural driver of a graded refinement that would close the enclosure faster.

3.4 Thin sheet in a three-layer stack

Problem 4 is a silicon stack representative of the isolation sheets of stacked-photodiode sensors [13, 14]: Region 1, 300 nm thick with $N_D = 10^{16}$ cm^{-3} ($\sigma = 200$ S m^{-1}), on a 30 nm sheet, on Region 3, 6 µm thick with $N_D = 10^{15}$ cm^{-3} ($\sigma = 21.6$ S m^{-1}). The sheet is either heavily doped, $N_D = 10^{17}$ cm^{-3} ($\sigma = 1280$ S m^{-1}), or lightly doped, $N_D = 10^{14}$ cm^{-3} ($\sigma = 2.16$ S m^{-1}). Conductivities follow from $\sigma = qN_D\mu_n$ with the electron mobilities 1350, 1250 and 800 cm^2 V^{-1} s^{-1} at $N_D = 10^{14}$–10^{15}, 10^{16} and 10^{17} cm^{-3}, from the

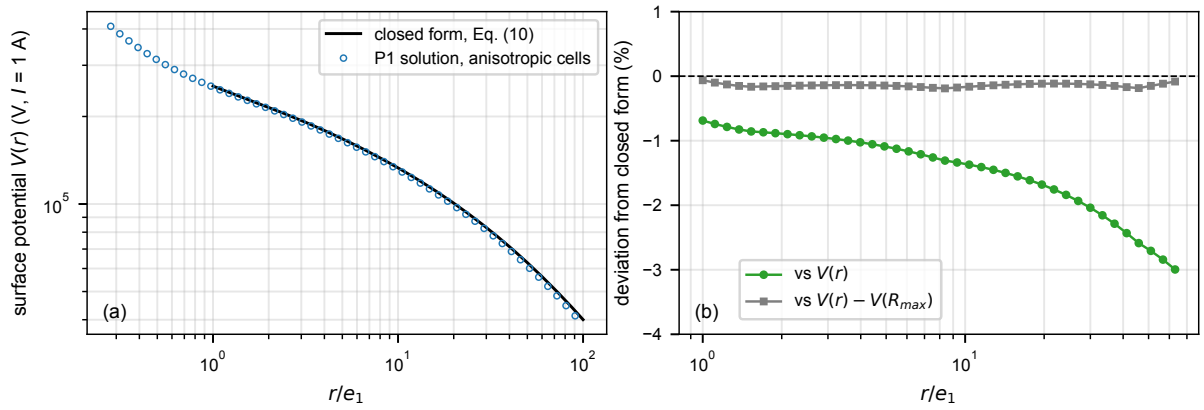


Fig. 4 Problem 2: point source on a 30 nm film ($\sigma_1 = 100\ \mathrm{S\,m^{-1}}$) over a substrate ($\sigma_2 = 1\ \mathrm{S\,m^{-1}}$). (a) Surface potential, P1 solution on anisotropic cells and closed form, Eq. (10). (b) Relative deviation from the closed form (circles) and from the closed form referred to its value at the grounded boundary $R_{\max} = 100$ µm (squares)

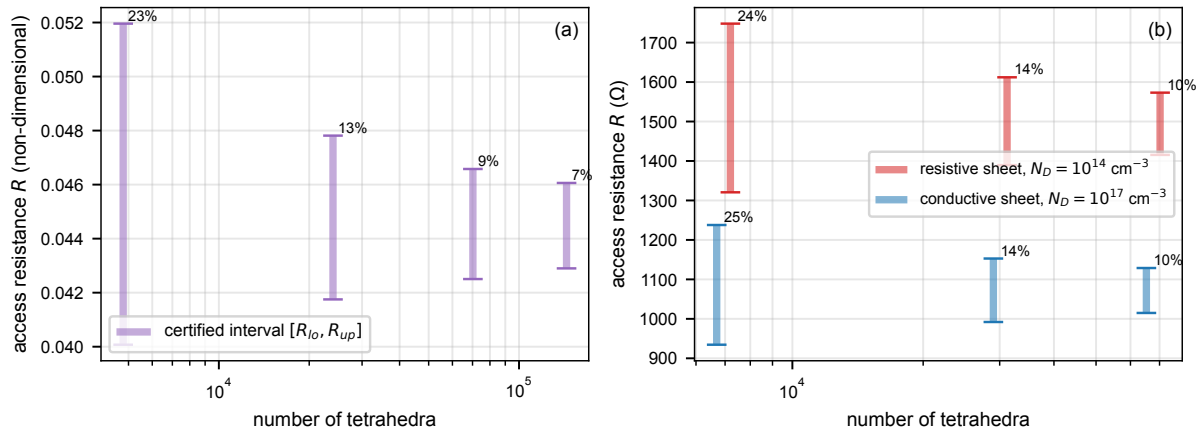


Fig. 5 Certified enclosures $[R_{\mathrm{lo}}, R_{\mathrm{up}}]$ of the access resistance under refinement, labelled with their width η. (a) Problem 3, film contact. (b) Problem 4, three-layer stack with the conductive (blue) and the resistive (red) sheet. Contact edges lie on grid lines for every mesh, so all intervals of a series enclose the same exact value; the two series are disjoint

Caughey–Thomas fit [40]. Fig. 6 shows the equilibrium band diagrams for context. The bands step down by $V_t \ln(N_{D1}/N_{D3}) \approx 60$ mV from Region 1 to Region 3. The heavily doped sheet pulls the conduction band down into a notch 42 meV below its level in Region 1. In the lightly doped sheet the conduction band lies 21 to 31 meV above that level, so part of the step falls across the sheet.

Current is injected through a 200 nm radius contact on top of Region 1 and collected 20 µm away. The axisymmetric mesh has 2754 nodes, with 4 cells across the sheet. Fig. 7 shows the potential along the injection axis. The heavily doped sheet carries 0.13% of the potential drop and acts as a shunt. The lightly doped sheet carries 13.4% and acts as a barrier. The access resistance changes from 16.3 kΩ to 18.4 kΩ, by 12.4%, although the sheet is 0.5% of the total thickness. A compact model that removes the sheet from the mesh cannot produce this difference without a calibration that would require the resolved simulation. The same conclusion holds with a guarantee on the three-dimensional version of the stack ($W = 10$ µm, square contact on grid lines), where both sheets are enclosed on the same three meshes (Table 3, Fig. 5b). The two enclosures are disjoint already on the coarsest mesh, 7200 tetrahedra, and on the finest they are $R \in [1015, 1129]$ Ω with the conductive sheet and $[1415, 1573]$ Ω with the resistive one. The resistive sheet raises the access

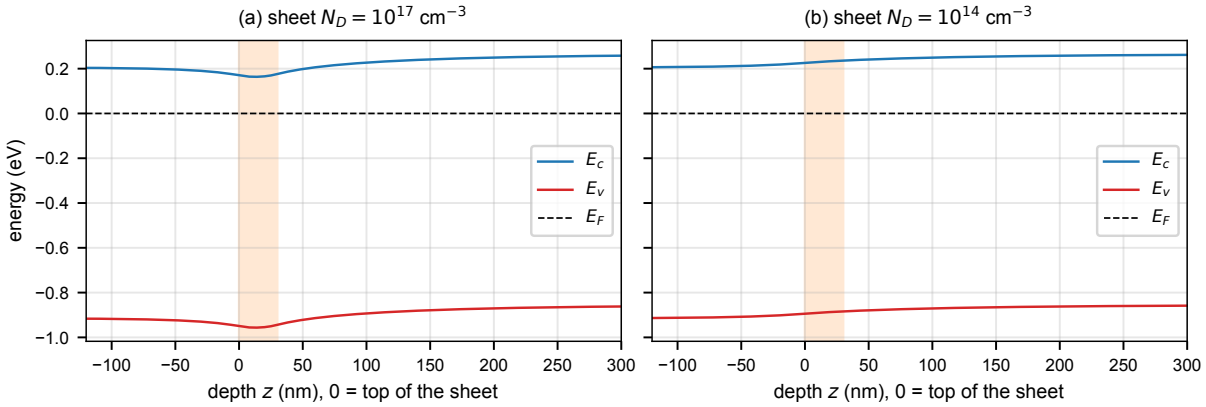


Fig. 6 Problem 4: equilibrium band diagrams of the stack, Region 1 ($N_D = 10^{16}$ cm^{-3}) / 30 nm sheet / Region 3 ($N_D = 10^{15}$ cm^{-3}), from the one-dimensional Poisson–Boltzmann equation. (a) Heavily doped sheet. (b) Lightly doped sheet. The Fermi level E_F is the energy origin

Table 3 Certified enclosures of the access resistance, Eq. (7). Problem 3 is non-dimensional; problem 4 in Ω

n_x	tetrahedra	R_{lo}	R_{up}	η (%)
Problem 3, film contact				
10	4800	0.04007	0.05196	22.9
20	24000	0.04175	0.04781	12.7
30	70200	0.04250	0.04658	8.7
40	144000	0.04290	0.04606	6.9
Problem 4, conductive sheet				
10	7200	934	1238	24.5
20	31200	992	1153	13.9
30	70200	1015	1129	10.1
Problem 4, resistive sheet				
10	7200	1321	1748	24.5
20	31200	1390	1612	13.8
30	70200	1415	1573	10.0

resistance by at least 25%, a lower bound that no compact model of the sheet could certify. The widths, 10.1% and 10.0% on 70200 tetrahedra, are those of the contact singularity, as in Section 3.3.

4 Discussion

Anisotropic a posteriori estimators of residual [21, 22] and recovery [18, 23] type are designed to drive mesh adaptation, and their reliability constants depend on how well the mesh is aligned with the solution. The complementary enclosure used here has no such constant: Eq. (7) holds on any conforming mesh, whatever the shape of its elements. Equilibrated-flux estimators share this property [28, 30–33]. They usually reconstruct the flux locally from the potential, whereas here it comes from a global mixed solve on the same mesh. That costs a second, larger linear system, for the face fluxes, and gives an exact flux whenever the RT0 space contains the exact current. The layer-parallel results of Section 3.1 rely on this property.

The enclosure concerns the conductance, or any quadratic output of Eq. (1), rather than the pointwise field. Pointwise quantities such as the potential at a given depth are reported here from the primal solution, and their accuracy follows from the validation of Section 3.2. A goal-oriented version of the enclosure would extend the guarantee to linear outputs. The nonlinear equilibrium of doped layers admits a different certificate, based on sub- and super-solutions and the monotone comparison principle [41], applied to the Poisson–Boltzmann equation [42]. That development, and its application to isolation barriers, is the subject of a companion paper.

The same anisotropic cells apply to thin-film test structures. For a thin-film Hall bar, the extracted geometry factor recovers the ideal transverse response and the classical finite-contact correction [43, 44] on cells stretched beyond 100:1. Combined with the enclosure of Eq. (7) on the sheet resistance, this gives certified extraction of thin-film transport parameters.

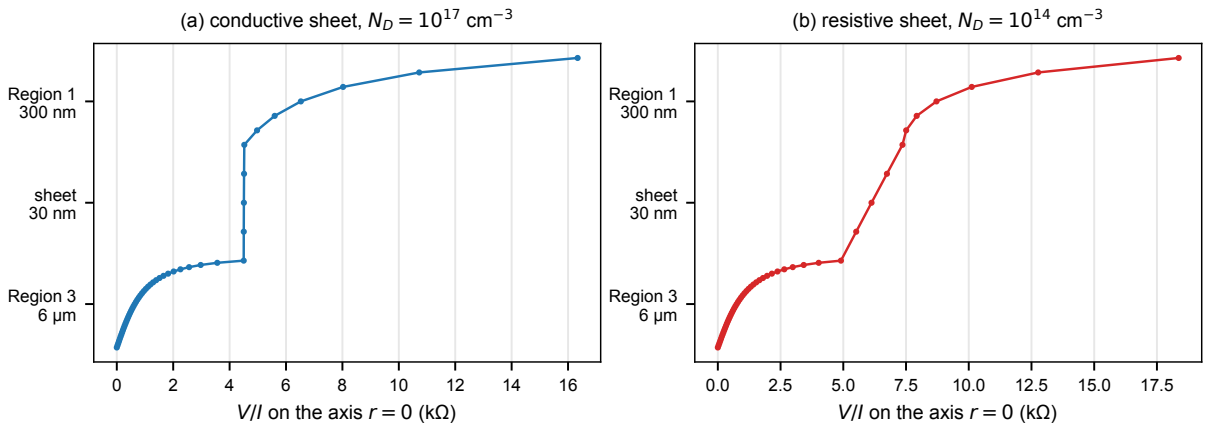


Fig. 7 Problem 4: potential per unit current along the injection axis, with the vertical scale expanded around the sheet. (a) Conductive sheet, 0.13% of the drop. (b) Resistive sheet, 13.4% of the drop

5 Conclusion

A thin, wide layer is a numerical bottleneck rather than a physical one. An isotropic mesher pays a cost quadratic in the layer aspect ratio, and 1.6×10^7 nodes for a 30 µm film on a 10 mm die, to resolve a thickness that the in-plane solution does not feel. Anisotropic structured cells make the cost independent of the aspect ratio. A conforming potential and an equilibrated Raviart–Thomas current, computed on the same mesh, then enclose the exact resistance between guaranteed bounds. The enclosure is exact to round-off for layer-parallel flow up to 1000:1. It reproduces the closed-form potential of a point source on a 30 nm film to within 0.14%. On a contact, it gives nested enclosures that shrink to 6.9%. Applied to a three-layer stack, it resolves a 30 nm sheet whose doping changes its share of the potential drop from 0.13% to 13.4%, and it certifies the difference: the enclosures of the access resistance for the two dopings do not overlap.

Declarations

- **Funding** The authors did not receive support from any organization for the submitted work.
- **Competing interests** The authors have no competing interests to declare that are relevant to the content of this article.
- **Author contributions** H. Talleb: conceptualization, methodology, software, validation, writing (original draft). A. Elomari: device structure, investigation, writing (review and editing). M. Ben Chouikha: device structure, supervision, writing (review and editing). All authors read and approved the final manuscript.
- **Data availability** No experimental data were used. All numerical data are generated by the scripts listed under Code availability.
- **Code availability** The Python scripts that produce every figure, table and number of this article are available at https://github.com/tallebhakeim/certified-anisotropic-meshing.

References

[1] Bank, R.E., Rose, D.J., Fichtner, W.: Numerical methods for semiconductor device simulation. IEEE Trans. Electron Devices **30**(9), 1031–1041 (1983) https://doi.org/10.1109/T-ED.1983.21257

[2] Selberherr, S.: Analysis and Simulation of Semiconductor Devices. Springer, Vienna (1984) https://doi.org/10.1007/978-3-7091-8752-4

[3] Giles, M.: TCAD process/device modeling challenges and opportunities for the next decade. J. Comput. Electron. **3**(3–4), 177–182 (2004) https://doi.org/10.1007/s10825-004-7040-2

[4] Fleischmann, P., Selberherr, S.: Enhanced advancing front Delaunay meshing in TCAD. In: Proc. Int. Conf. Simulation of Semiconductor Processes and Devices (SISPAD), pp.

99–102. IEEE, Kobe (2002) https://doi.org/10.1109/SISPAD.2002.1034526

[5] Frey, P.J., George, P.-L.: Mesh Generation: Application to Finite Elements, 2nd edn. ISTE, London; Wiley, Hoboken (2008) https://doi.org/10.1002/9780470611166

[6] Babuška, I., Aziz, A.K.: On the angle condition in the finite element method. SIAM J. Numer. Anal. **13**(2), 214–226 (1976) https://doi.org/10.1137/0713021

[7] Křížek, M.: On the maximum angle condition for linear tetrahedral elements. SIAM J. Numer. Anal. **29**(2), 513–520 (1992) https://doi.org/10.1137/0729031

[8] Kosik, R., Fleischmann, P., Haindl, B., Pietra, P., Selberherr, S.: On the interplay between meshing and discretization in three-dimensional diffusion simulation. IEEE Trans. Comput.-Aided Des. Integr. Circuits Syst. **19**(11), 1233–1240 (2000) https://doi.org/10.1109/43.892848

[9] Ismail, M., Sarker, M., Mohamed, M., Kim, J.: Moving mesh adaptation for Si and GaN-based power device simulation. J. Comput. Electron. **17**(4), 1621–1629 (2018) https://doi.org/10.1007/s10825-018-1218-5

[10] Colinge, J.-P. (ed.): FinFETs and Other Multi-Gate Transistors. Springer, New York (2008) https://doi.org/10.1007/978-0-387-71752-4

[11] Radisavljevic, B., Radenovic, A., Brivio, J., Giacometti, V., Kis, A.: Single-layer MoS_2 transistors. Nat. Nanotechnol. **6**(3), 147–150 (2011) https://doi.org/10.1038/nnano.2010.279

[12] Fortunato, E., Barquinha, P., Martins, R.: Oxide semiconductor thin-film transistors: a review of recent advances. Adv. Mater. **24**(22), 2945–2986 (2012) https://doi.org/10.1002/adma.201103228

[13] Ben Chouikha, M., Dubois, G.: Capteur multi-spectral à photodétecteurs empilés. French Patent FR3060848A1 (2018)

[14] Elomari, A.: Étude et développement d'un procédé de fabrication de photodétecteur couleur et multispectral. PhD thesis, Sorbonne Université, Paris (2024). https://theses.hal.science/tel-05081767

[15] Smits, F.M.: Measurement of sheet resistivities with the four-point probe. Bell Syst. Tech. J. **37**(3), 711–718 (1958) https://doi.org/10.1002/j.1538-7305.1958.tb03883.x

[16] Schroder, D.K.: Semiconductor Material and Device Characterization, 3rd edn. Wiley, Hoboken (2006) https://doi.org/10.1002/0471749095

[17] Apel, T.: Anisotropic Finite Elements: Local Estimates and Applications. Teubner, Stuttgart (1999)

[18] Formaggia, L., Perotto, S.: New anisotropic a priori error estimates. Numer. Math. **89**(4), 641–667 (2001) https://doi.org/10.1007/s002110100273

[19] Frey, P.J., Alauzet, F.: Anisotropic mesh adaptation for CFD computations. Comput. Methods Appl. Mech. Eng. **194**(48–49), 5068–5082 (2005) https://doi.org/10.1016/j.cma.2004.11.025

[20] Loseille, A., Alauzet, F.: Continuous mesh framework part I: well-posed continuous interpolation error. SIAM J. Numer. Anal. **49**(1), 38–60 (2011) https://doi.org/10.1137/090754078

[21] Kunert, G.: An a posteriori residual error estimator for the finite element method on anisotropic tetrahedral meshes. Numer. Math. **86**(3), 471–490 (2000) https://doi.org/10.1007/s002110000170

[22] Kunert, G., Verfürth, R.: Edge residuals dominate a posteriori error estimates for linear finite element methods on anisotropic triangular and tetrahedral meshes. Numer. Math. **86**(2), 283–303 (2000) https://doi.org/10.1007/PL00005407

[23] Picasso, M.: An anisotropic error indicator based on Zienkiewicz–Zhu error estimator: application to elliptic and parabolic problems. SIAM J. Sci. Comput. **24**(4), 1328–1355 (2003) https://doi.org/10.1137/S1064827501398578

[24] Synge, J.L.: The Hypercircle in Mathematical Physics. Cambridge University Press, Cambridge (1957)

[25] Prager, W., Synge, J.L.: Approximations in elasticity based on the concept of function space. Q. Appl. Math. **5**(3), 241–269 (1947) https://doi.org/10.1090/qam/25902

[26] Hammond, P., Penman, J.: Calculation of inductance and capacitance by means of dual energy principles. Proc. IEE **123**(6), 554–559 (1976) https://doi.org/10.1049/piee.1976.0125

[27] Rikabi, J., Bryant, C.F., Freeman, E.M.: An error-based approach to complementary formulations of static field solutions. Int. J. Numer. Methods Eng. **26**(9), 1963–1987 (1988) https://doi.org/10.1002/nme.1620260906

[28] Ladevèze, P., Leguillon, D.: Error estimate procedure in the finite element method and applications. SIAM J. Numer. Anal. **20**(3), 485–509 (1983) https://doi.org/10.1137/0720033

[29] Destuynder, P., Métivet, B.: Explicit error bounds in a conforming finite element method. Math. Comput. **68**(228), 1379–1396 (1999) https://doi.org/10.1090/S0025-5718-99-01093-5

[30] Braess, D., Schöberl, J.: Equilibrated residual error estimator for edge elements. Math. Comput. **77**(262), 651–672 (2008) https://doi.org/10.1090/S0025-5718-07-02080-7

[31] Braess, D., Pillwein, V., Schöberl, J.: Equilibrated residual error estimates are p-robust. Comput. Methods Appl. Mech. Eng. **198**(13–14), 1189–1197 (2009) https://doi.org/10.1016/j.cma.2008.12.010

[32] Vohralík, M.: Guaranteed and fully robust a posteriori error estimates for conforming discretizations of diffusion problems with discontinuous coefficients. J. Sci. Comput. **46**(3), 397–438 (2011) https://doi.org/10.1007/s10915-010-9410-1

[33] Ern, A., Vohralík, M.: Polynomial-degree-robust a posteriori estimates in a unified setting for conforming, nonconforming, discontinuous Galerkin, and mixed discretizations. SIAM J. Numer. Anal. **53**(2), 1058–1081 (2015) https://doi.org/10.1137/130950100

[34] Repin, S.: A Posteriori Estimates for Partial Differential Equations. De Gruyter, Berlin (2008) https://doi.org/10.1515/9783110203042

[35] Bey, J.: Simplicial grid refinement: on Freudenthal's algorithm and the optimal number of congruence classes. Numer. Math. **85**(1), 1–29 (2000) https://doi.org/10.1007/s002110050475

[36] Raviart, P.-A., Thomas, J.-M.: A mixed finite element method for 2-nd order elliptic problems. In: Galligani, I., Magenes, E. (eds.) Mathematical Aspects of Finite Element Methods. Lect. Notes Math., vol. 606, pp. 292–315. Springer, Berlin (1977) https://doi.org/10.1007/BFb0064470

[37] Boffi, D., Brezzi, F., Fortin, M.: Mixed Finite Element Methods and Applications. Springer, Berlin (2013) https://doi.org/10.1007/978-3-642-36519-5

[38] Ren, Z.: A 3D vector potential formulation using edge element for electrostatic field computation. IEEE Trans. Magn. **31**(3), 1520–1523 (1995) https://doi.org/10.1109/20.376319

[39] Tonti, E.: Finite formulation of the electromagnetic field. Prog. Electromagn. Res. **32**, 1–44 (2001) https://doi.org/10.2528/PIER00080101

[40] Caughey, D.M., Thomas, R.E.: Carrier mobilities in silicon empirically related to doping and field. Proc. IEEE **55**(12), 2192–2193

(1967) https://doi.org/10.1109/PROC.1967.6123

[41] Sattinger, D.H.: Monotone methods in nonlinear elliptic and parabolic boundary value problems. Indiana Univ. Math. J. **21**(11), 979–1000 (1972) https://doi.org/10.1512/iumj.1972.21.21079

[42] Markowich, P.A.: The Stationary Semiconductor Device Equations. Springer, Vienna (1986) https://doi.org/10.1007/978-3-7091-3678-2

[43] Wick, R.F.: Solution of the field problem of the germanium gyrator. J. Appl. Phys. **25**(6), 741–756 (1954) https://doi.org/10.1063/1.1721725

[44] Lippmann, H.J., Kuhrt, F.: Der Geometrieeinfluß auf den Hall-Effekt bei rechteckigen Halbleiterplatten. Z. Naturforsch. A **13**(6), 474–483 (1958) https://doi.org/10.1515/zna-1958-0608